AGU ADVANCING EARTH AND SPACE SCIENCES

Earth and Space Science

RESEARCH ARTICLE
10.1029/2025EA004203

A Microphysics Model of Multicomponent Venus' Clouds With a High-Accuracy Condensation Scheme

H. Karyu[1,2,3], T. Kuroda[1,4], A. Mahieux[2], S. Viscardy[2], A. Määttänen[5], N. Terada[1], S. Robert[2], A. C. Vandaele[2], and M. Crucifix[3]

[1]Department of Geophysics, Tohoku University, Sendai, Japan, [2]Royal Belgian Institute for Space Aeronomy, (BIRA-IASB), Brussels, Belgium, [3]Earth and Life Institute, Université Catholique de Louvain, Louvain-la-Neuve, Belgium, [4]Division for the Establishment of Frontier Sciences of Organization for Advanced Studies, Tohoku University, Sendai, Japan, [5]LATMOS, IPSL, CNRS, Sorbonne Université, UVSQ Université Paris-Saclay, Paris, France

Key Points:

- The moving-center bin scheme is applied for the first time in a Venus cloud microphysics model
- The new model accurately simulates the Venusian clouds by minimizing numerical diffusion, successfully reproducing the observed structures
- Halving the resolution cut computation time sixfold, keeping accuracy intact, proving the model's potential for future 3-D modeling

Supporting Information:

Supporting Information may be found in the online version of this article.

Correspondence to:

H. Karyu,
hiroki.karyu.q4@dc.tohoku.ac.jp

Citation:

Karyu, H., Kuroda, T., Mahieux, A., Viscardy, S., Määttänen, A., Terada, N., et al. (2025). A microphysics model of multicomponent Venus' clouds with a high-accuracy condensation scheme. *Earth and Space Science*, *12*, e2025EA004203. https://doi.org/10.1029/2025EA004203

Received 5 JAN 2025
Accepted 30 MAY 2025

Author Contributions:

Conceptualization: H. Karyu, T. Kuroda, A. Mahieux, S. Viscardy, A. Määttänen
Data curation: H. Karyu
Formal analysis: H. Karyu
Funding acquisition: H. Karyu, T. Kuroda, N. Terada
Investigation: H. Karyu
Methodology: H. Karyu, T. Kuroda, A. Mahieux, S. Viscardy, A. Määttänen
Project administration: T. Kuroda, N. Terada, A. C. Vandaele
Resources: T. Kuroda, N. Terada, S. Robert, A. C. Vandaele
Software: H. Karyu
Supervision: T. Kuroda, N. Terada, S. Robert, A. C. Vandaele, M. Crucifix

Abstract Accurate modeling of the Venusian cloud structure remains challenging due to its complex microphysical properties. Condensation primarily determines the cloud particle size distribution within the various cloud layers. However, existing Venus microphysics models mainly use a full-stationary bin scheme, which may be prone to numerical diffusion during condensation. To address this, we developed a new microphysics model, the Simulator of Particle Evolution, Composition, and Kinetics (SPECK), which incorporates a moving-center bin scheme designed to minimize numerical diffusion. Furthermore, SPECK can accommodate any number of size distributions with multiple components, enabling versatile applications for more complex cloud systems. The 0-D simulations demonstrated that this microphysics framework is a reliable tool for modeling cloud microphysics under Venusian atmospheric conditions, particularly in capturing condensation and evaporation processes. We further validated SPECK against recent Venus microphysics models in 1-D simulations. The moving-center scheme is shown to exhibit less numerical diffusion compared to an existing model based on a full-stationary bin scheme, allowing for more accurate calculations of microphysical processes. Furthermore, SPECK reproduces the cloud structure observed by the Pioneer Venus Large Probe, using the same computational settings adopted in the latest microphysical model study. Thanks to the suppressed numerical diffusion, SPECK achieves high accuracy at half the typical resolution while reducing computational time sixfold, making it a promising tool for future 3-D modeling. This microphysics framework will be useful for the upcoming EnVision mission and is applicable to other planetary atmospheres, including those of Mars, Titan, gas giants, and exoplanets.

Plain Language Summary Understanding the cloud structure on Venus is challenging due to the complex interaction between cloud particles and the atmosphere. A major process shaping these clouds is condensation, which affects the size of particles in the clouds. However, existing models of the Venusian clouds often struggle with accuracy due to a method that can cause errors in the simulation of the condensation process. To address this, we developed a new model, the Simulator of Particle Evolution, Composition, and Kinetics (SPECK), which reduces these errors, allowing for more precise predictions of how particles change in size. SPECK also works with a wide range of particle types, making it adaptable for studying other complex cloud systems. In simple box simulations, SPECK proved effective for modeling cloud processes on Venus, especially in tracking how particles grow and evaporate. The model also successfully reproduces observations from the Pioneer Venus Large Probe, showing better accuracy than previous methods while requiring less computing power. This makes SPECK a valuable tool for future Venus studies, including the upcoming EnVision mission. Additionally, SPECK can be applied to study clouds on other planets, such as Mars, Titan, gas giants, and exoplanets.

1. Introduction

Aerosols composing the clouds in Venus' atmosphere are essential for understanding the climate and its evolution. These particles reflect incoming solar radiation and trap outgoing near-infrared radiation, collectively exerting a significant influence on the energy balance of the planet (Limaye et al., 2018). Furthermore, recent findings by Mahieux et al. (2024) suggest that water-containing aerosols may play a critical role in the vertical transport of water vapor to the thermosphere, where interactions with atmospheric escape processes contribute to water loss (e.g., Chaffin et al., 2024; Gillmann et al., 2022). This offers clues to the ancient water inventory of Venus and the

Validation: H. Karyu
Visualization: H. Karyu
Writing – original draft: H. Karyu
Writing – review & editing: T. Kuroda, A. Mahieux, S. Viscardy, A. Määttänen, N. Terada, S. Robert, A. C. Vandaele, M. Crucifix

possibility of past Earth-like conditions. Thus, accurate characterization of aerosols is essential for reconstructing Venus' climatic and atmospheric history and unraveling the mechanisms that shaped its current extreme environment.

Clouds, in general, and Venusian clouds in particular, can be characterized by the size distribution of particles. The standard Venusian cloud structure consists of four distinct layers, each with different size distributions: the lower, middle, and upper clouds, and the upper haze (Knollenberg & Hunten, 1980; Titov et al., 2018). The structure of the three main cloud layers was established by the Large Probe Cloud Particle Size spectrometer (LCPS) on Pioneer Venus (PV) (Knollenberg & Hunten, 1980). The lower and middle cloud layers, located between 48 and 57 km, exhibit a size distribution with three modal radii: Mode 1 (∼0.15–0.2 μm), Mode 2 (∼1–1.3 μm), and Mode 3 (∼3.5 μm). The upper cloud layer, located between 57 and 70 km, displays a bimodal size distribution consisting of Mode 1 and Mode 2 particles. The upper haze layer lies above the upper cloud, and observations conducted by Solar Occultation in the InfraRed (SOIR) instrument onboard Venus Express (VEx) confirmed that this layer extends up to ∼100 km (Takagi et al., 2019; Wilquet et al., 2009, 2012). The primary composition of the particles in these four layers is a binary mixture of sulfuric acid (H_2SO_4) and water (H_2O) (Young, 1973). Throughout this paper, the term “cloud particle” refers specifically to particles within the cloud layers, while the term “aerosol” is used to describe all atmospheric particles, including particles in the cloud and haze layers.

Aerosol microphysics models are an effective tool for studying the size distribution of the Venusian cloud. (e.g., Gao et al., 2014; Imamura & Hashimoto, 2001; James et al., 1997; Karyu et al., 2024; McGouldrick & Barth, 2023; McGouldrick & Toon, 2007). Sectional models use discrete size bins to represent the particle population, offering more accurate solutions to condensation and coagulation processes. The Community Aerosol and Radiation Model for Atmospheres (CARMA) (Toon et al., 1988; Turco et al., 1979) has been used in the Venusian cloud studies, providing valuable insights into the formation of cloud holes (McGouldrick & Toon, 2007), bimodal structure in the upper haze (Gao et al., 2014), and the effects of coagulation on cloud variability (McGouldrick, 2017; McGouldrick & Barth, 2023). Imamura and Hashimoto (2001) developed a cloud microphysics model incorporating updraft effects, and with this model, they demonstrated that a trimodal distribution can form through mixing within the cloud layer. Recently, Karyu et al. (2024) (hereafter K2024) reproduced the observed cloud structure and condensational vapor profiles simultaneously, using a microphysics model based on that of Imamura and Hashimoto (2001).

All models mentioned above use a full-stationary bin scheme, which is mainstream in the current planetary science community. The particle size associated with each bin is constant in this scheme. However, various approaches have been developed in terrestrial aerosol studies since the creation of CARMA (Toon et al., 1988; Turco et al., 1979), and planetary microphysics models can benefit from these approaches. For instance, the moving-center scheme, in which particle size can vary within each bin, is widely used in terrestrial aerosol research because it can calculate condensation processes with higher accuracy (e.g., Bergman et al., 2012; Fast et al., 2006; Jacobson et al., 2007; Mann et al., 2012; Matsui, 2017). This method could also be useful for Venusian cloud studies because the formation of the main cloud deck is driven by rapid condensation, and to the best of our knowledge, has never been used in planetary studies.

Furthermore, on Earth, aerosols contain multiple components, and their mixing state is essential for understanding their impact on climate, atmospheric chemistry, and human health (Riemer et al., 2019 and references therein). Although the aerosol mixing state may affect the atmospheric radiation and chemical processes on Venus as well, the existing models for Venus consider at most 2 types of distributions consisting of single Cloud Condensation Nucleus (CCN) material and H_2SO_4-H_2O droplets. In addition, the upcoming EnVision mission is anticipated to further reveal the characteristics of Venusian aerosols (ESA, 2023). Therefore, versatility in accounting for various substances and different types of aerosol distributions would be essential in microphysics modeling.

In this paper, we present our newly developed aerosol microphysics model called the Simulator of Particle Evolution, Composition, and Kinetics (SPECK). The moving-center bin scheme has been implemented for the first time in planetary aerosol studies. This model also incorporates multiple size distributions, each with multiple components, and accounts for mixing between independent size distributions.

The paper is organized as follows. In Section 2, we introduce our new microphysics model and the equations it is based on. In Section 3, we perform 0-D simulations to evaluate the performance of the microphysics framework.

In Section 4, we perform 1-D simulations using settings consistent with previous work to validate our model including transport. Finally, conclusions and future prospects are presented in Section 5.

2. Model Description

2.1. Overview

SPECK computes the vertical distributions of particle components, such as solid CCN materials and liquid components, and gas species using the 1-D continuity equation. The particle components are represented by multiple size distributions, each divided into size bins. Interactions between these distributions are also incorporated. The 1-D continuity equation for each aerosol component is expressed as follows (modified from Toon et al. (1988)).

$$\frac{\partial c_{q,N_i}(z,t)}{\partial t} = \frac{\partial}{\partial z}\left(K_{\text{eddy}}(z)\, n_{\text{air}}(z)\, \frac{\partial}{\partial z}\left[\frac{c_{q,N_i}(z,t)}{n_{\text{air}}(z)}\right]\right) - \frac{\partial}{\partial z}\left[w_{\text{sed}}(v_{N_i}, z)\, c_{q,N_i}(z,t)\right] + \left[\frac{\partial c_{q,N_i}(z,t)}{\partial t}\right]_{\text{cond}} + \left[\frac{\partial c_{q,N_i}(z,t)}{\partial t}\right]_{\text{coag}} \tag{1}$$

where c_{q,N_i} is the concentration (mol m^{-3}) of particle component q in size bin i of distribution N at the altitude z (m) and time t (s), $n_{\text{air}}(z)$ is the air concentration (mol m^{-3}), $K_{\text{eddy}}(z)$ is the vertical eddy diffusion coefficient ($m^2\ s^{-1}$) of air, and $w_{\text{sed}}(v_{N_i}, z)$ is the sedimentation velocity (m s^{-1}) of aerosol particles with volume v_{N_i} (m^3). The symbol N used in Equation 1 refers to the type of particle species, such as CCN and H_2SO_4 liquid droplets, and so on. The configuration of particle species and their interactions is described in Section 2.4. The sedimentation velocity is expressed as follows (Pruppacher & Klett, 1997).

$$w_{\text{sed}} = \frac{2r(v_{N_i})^2 \rho_{\text{p}} g}{9\eta}\left[1 + \text{Kn}(z)\left\{A + B\exp\left(-\frac{C}{\text{Kn}(z)}\right)\right\}\right] \tag{2}$$

where $r(v_{N_i})$ is the particle radius (m) corresponding to the volume v_{N_i}, ρ_{p} is the density (kg m^{-3}) of the particle, $g = 8.7\ \text{m}\ \text{s}^{-2}$ is the gravitational acceleration of Venus, $\eta = 1.5 \times 10^{-5}\ \text{kg}\ \text{m}^{-1}\ \text{s}^{-1}$ is the viscosity of CO_2 gas, $\text{Kn}(z)$ is the Knudsen number for air, and the constants A, B, and C are experimental parameters set to be 1.249, 0.42, and 0.87, respectively, following Kasten (1968). The first term on the right-hand side of Equation 1 represents vertical transport by eddy diffusion. The second term accounts for vertical transport due to particle sedimentation. The third term, $\left[\frac{\partial c_{q,N_i}}{\partial t}\right]_{\text{cond}}$, and the fourth term, $\left[\frac{\partial c_{q,N_i}}{\partial t}\right]_{\text{coag}}$, are the rates of change in particle component q in size bin i of distribution N due to condensation and coagulation, respectively. These microphysics terms will be explained in Sections 2.3 and 2.4. Similarly, the 1-D continuity equation for gas species is represented as follows

$$\frac{\partial C_q(z,t)}{\partial t} = \frac{\partial}{\partial z}\left(K_{\text{eddy}}(z)\, n_{\text{air}}(z)\, \frac{\partial}{\partial z}\left[\frac{C_q(z,t)}{n_a(z)}\right]\right) + \left[\frac{\partial C_q(z,t)}{\partial t}\right]_{\text{cond}} + \left[\frac{\partial C_q(z,t)}{\partial t}\right]_{\text{chem}} \tag{3}$$

where C_q is the concentration (mol m^{-3}) of gas component q, $\left[\frac{\partial C_q}{\partial t}\right]_{\text{cond}}$ and $\left[\frac{\partial C_q}{\partial t}\right]_{\text{chem}}$ are the rates of change in gas concentration due to condensation and chemistry.

We consider three particle components with $q = 1$ for H_2SO_4, $q = 2$ for H_2O, and $q = 3$ for CCN, following previous microphysics studies (e.g., Gao et al., 2014; McGouldrick, 2017; McGouldrick & Barth, 2023). These particle components are further categorized as either condensable or dry species in the model. The condensable species, H_2SO_4 and H_2O, are exchanged between particles and gas phases depending on the saturation vapor pressure. In contrast, the dry species, CCN, is non-condensable and remains only within the solid particle phase. The CCN material is assumed to be elemental sulfur and insoluble, following the previous microphysical studies (Gao et al., 2014; Imamura & Hashimoto, 2001; McGouldrick, 2017).

We consider three types of particle distributions based on their components. The first is the CCN distribution, which consists solely of CCN particle component, supplied by the formation of elemental sulfur. The second is the

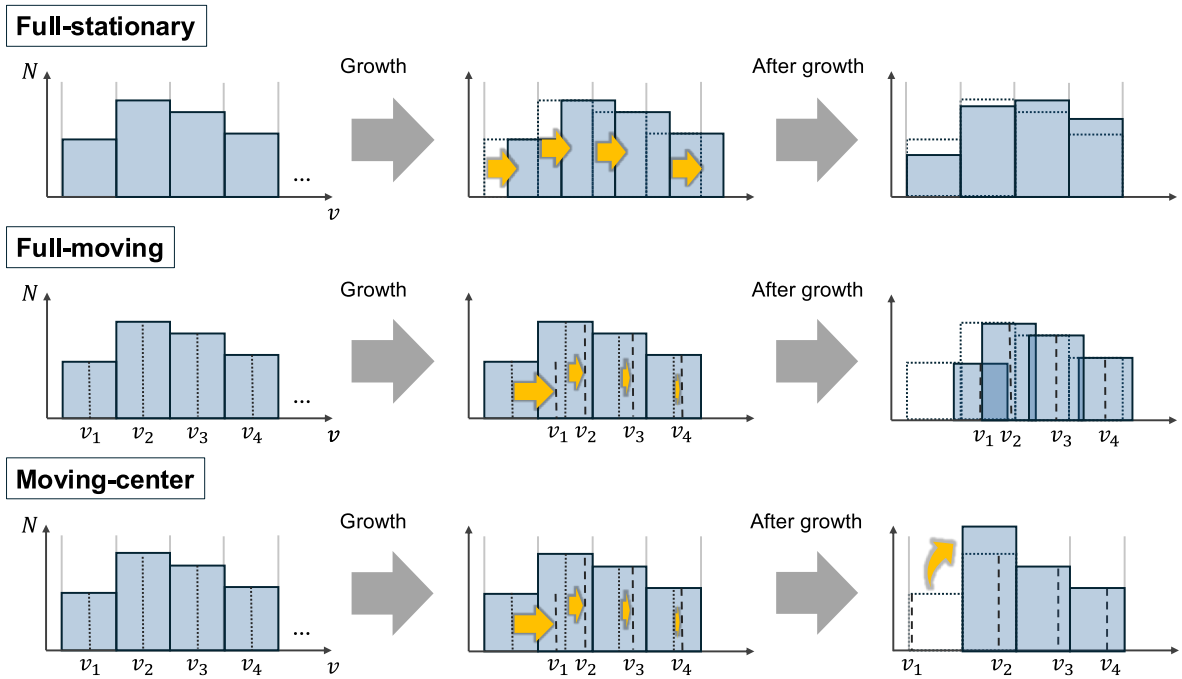

Figure 1. A schematic illustration of the full-stationary (top row), full-moving (middle row), and moving-center (bottom row) schemes. The left column represents the initial size distribution as a function of volume, with gray lines marking fixed bin boundaries in the full-stationary and moving-center schemes. Characteristic volumes v_{1-4} are assigned to bins in the full-moving and moving-center schemes. The middle column depicts the treatment of growth in each bin scheme: yellow arrows in the full-stationary scheme indicate advection in size space, while in the full-moving and moving-center schemes, they represent growth to the exact volume. The right column shows the predicted size distributions after the growth process. The hatched distribution corresponds to the original size distribution. In the moving-center scheme, all number density from the first bin is transferred to the next larger size bin when the characteristic volume exceeds the upper boundary of the bin. Note that this figure is intended only to illustrate the calculation concept and does not represent actual calculation results.

sulfuric acid droplet distribution, comprising a binary mixture of H_2SO_4 and H_2O. The third type is the mixed distribution, which includes both CCN and sulfuric acid droplets. Mixed particles form either when CCN particles become wetted or when CCN and sulfuric acid droplets undergo coagulation.

The particle bin structure is constructed based on a volume-ratio size distribution, designed to cover a size range spanning several orders of magnitude (Jacobson, 1997a). The high-edge volume ($v_{i,\mathrm{hi}}$) of the ith bin is determined by multiplying the low-edge volume ($v_{i,\mathrm{lo}}$) by V_{rat} which is a constant volume ratio between adjacent bins and can take any value greater than one. Accordingly, the volume width of a size bin (dv_i) is expressed as

$$\begin{aligned} dv_i &= v_{i,\mathrm{hi}} - v_{i,\mathrm{lo}} \\ &= V_{\mathrm{rat}} v_{i,\mathrm{lo}} - v_{i,\mathrm{lo}} \\ &= (V_{\mathrm{rat}} - 1)\, v_{i,\mathrm{lo}} \end{aligned} \tag{4}$$

Throughout the simulation, dv_i, $v_{i,\mathrm{lo}}$, and $v_{i,\mathrm{hi}}$ are fixed, while particle volume v_i can vary between the edges of the respective bins $v_{i,\mathrm{lo}}$ and $v_{i,\mathrm{hi}}$, as explained in the Section 2.2.

2.2. Bin Scheme

The performance of the sectional microphysics model heavily depends on the choice of bin scheme, as each scheme has its advantages and disadvantages. Figure 1 shows three common bin schemes used in aerosol microphysics simulations. The scheme widely used in planetary microphysics models is the full-stationary scheme (e.g., Karyu et al., 2024; McGouldrick & Barth, 2023; Toon et al., 1988; Turco et al., 1979). In this scheme, average particle sizes and bin boundaries are fixed throughout the simulation, making it convenient for nucleation, coagulation, and transport in multiple dimensions. However, one drawback of this scheme is the

numerical diffusion of the size distribution during condensation because size growth is treated as Eulerian advection of number density within the size space.

The full-moving scheme is nearly the opposite of the full-stationary scheme, in the sense that the size bin boundaries themselves shift during the growth process (Gelbard, 1990). In a full-moving scheme, the particle radius assigned to each bin increases during growth, while the number density within each bin remains constant (Figure 1). This approach can be understood as Lagrangian advection within size space, providing an exact solution for condensational growth. However, this scheme is less practical for multi-dimensional studies, as each grid cell may have a distinct bin structure.

The bin scheme applied in this study is the moving-center scheme (Jacobson, 1997a). In the moving-center scheme, the boundaries of each size bin are fixed, but particle size can vary within each bin, as shown in Figure 1. As growth occurs, particles are allowed to grow to their exact sizes, which is identical to the full-moving scheme, making the growth calculation equivalent to Lagrangian advection in size space.

Once the particle size surpasses the upper boundary of a bin (corresponding to v_1 in the right column of Figure 1), the number density of that bin is transferred to the next larger bin. After this transfer, a pit structure may form within the size distribution due to the emptying of a size bin, creating an artificial pit in the distribution. The volume of the emptied bin (v_1) is then re-initialized to the lower edge of the bin. Meanwhile, the volume of the receiving bin (v_2) is updated to the average of the transferred particle sizes (v_1) and the pre-existing particle sizes (v_2) in that bin. The treatment of evaporation is numerically identical to that of condensation in the moving-center scheme. Thus, when the particle size crosses the lower boundary of a bin, the number density of that bin is transferred to the next smaller bin.

The volumes of other bins (v_3 and v_4), which do not experience growth or number density transfer, are preserved and integrated until their volumes surpass the boundaries of the respective bins. The formation of the pit is a drawback of the moving-center scheme. However, despite this pit formation, the algorithm has been shown to produce results nearly identical to the full-moving scheme because numerical diffusion is nearly eliminated in this scheme (Jacobson, 1997a, 2005). As a result, the moving-center scheme offers a more accurate solution for condensational growth compared to other sectional bin schemes (Jacobson, 1997a; Zhang et al., 1999). Furthermore, this scheme is easily coupled with nucleation, coagulation, and transport in multiple dimensions, as the bin boundaries remain fixed. Thus, the moving-center scheme can be regarded as a combination of the full-stationary and full-moving schemes.

2.3. Condensation Scheme

We consider two condensable species, with $q = 1$ for H_2SO_4 and $q = 2$ for H_2O. The condensational growth rate is calculated for H_2SO_4, while the condensation rate of H_2O is determined based on thermodynamic equilibrium adjustments. These adjustments depend on the surrounding temperature and available water vapor, following previous microphysical studies (Imamura & Hashimoto, 2001; Karyu et al., 2024; McGouldrick & Barth, 2023; McGouldrick & Toon, 2007). In the moving-center scheme, particle number density is not transferred between bins as size-space advection. Instead, particles grow precisely to their actual sizes during condensation, with number density transfer occurring after updating the size.

The condensational growth of particles and gas conservation are expressed as follows (Jacobson, 1997b).

$$\left[\frac{\partial c_{q,i}}{\partial t}\right]_{\text{cond}} = k_{q,i}(C_q - S_{q,i}C_{q,s}) \quad i = 1,\ldots,N_{\text{B}} \tag{5}$$

$$\left[\frac{\partial C_q}{\partial t}\right]_{\text{cond}} = -\sum_{i=1}^{N_{\text{B}}} k_{q,i}(C_q - S_{q,i}C_{q,s}) \tag{6}$$

where N_{B} is the total number of bins, $C_{q,s}$ is the saturation mole concentration (mol m^{-3}) of a vapor over a flat surface, $k_{q,i}$ is the mass transfer rate (s^{-1}) between the gas phase and all particles of size i, $S_{q,i}$ is the equilibrium saturation ratio of the condensing gas. The saturation vapor pressure for pure H_2SO_4 is taken from Kulmala and

Laaksonen (1990), and that for H_2O is taken from Eisenberg and Kauzmann (1969). The mass transfer rate $k_{q,i}$ is represented as $4\pi n_i r_i D_{q,i}^{\text{eff}}$, where n_i is the concentration of particles (m^{-3}) of the ith bin, r_i is the particle radius (m) of the ith bin, and $D_{q,i}^{\text{eff}}$ is an effective molecular diffusion coefficient ($m^2\ s^{-1}$) given by Jacobson (2005). The equilibrium saturation ratio $S_{q,i}$ is expressed as follows (Seinfeld & Pandis, 2016).

$$S_{q,i} = \exp\left(\frac{2\sigma_p m_w}{r_i RT\rho_{w,i}} + \frac{\mu_q(T,x) - \mu_q^o(T)}{RT}\right) \tag{7}$$

where σ_p is the average particle surface tension (kg s^{-2}), m_w is the average molar weight (kg mol^{-1}) of solution, R is the universal gas constant (J mol^{-1} K^{-1}), T is the temperature (K), $\rho_{w,i}$ is the density (kg m^{-3}) of the solution, $\mu_q(T,x)$ is the chemical potential (J mol^{-1}) of the condensing gas in the H_2SO_4-H_2O binary solution with H_2SO_4 mole fraction of x at temperature T, and $\mu_q^o(T)$ is the chemical potential (J mol^{-1}) of the pure solution. The first term in the exponential accounts for the Kelvin effect, while the second term represents the activity of the mixed solution. We used the parameterization of Vehkamäki et al. (2002) for σ_p as a function of the temperature and weight concentration of H_2SO_4 in the binary solution. The chemical potentials for the binary solution and pure H_2SO_4 are taken from Zeleznik (1991). The wetting of the CCN particles occurs when $C_q > S_{q,i}C_{q,s}$ since a detailed heterogeneous nucleation process is not included in this study. Accordingly, particle transfer between different size distributions is also computed. Particles in the CCN distribution participate in the mixed size distribution once they obtain a liquid component by condensational growth. Conversely, particles in the mixed distribution are transferred to the CCN distribution when they lose all the liquid components.

In general, soluble and insoluble cores play an important role in determining the saturation ratio, as the solute reduces the saturation vapor pressure, and the presence of a core modifies the volume of the liquid shell available to the solute (Petters & Kreidenweis, 2007). In the present simulation, we do not take into account these effects, as the CCN material is assumed to be perfectly insoluble, and thus, the solute effect is negligible. However, the impact of solubility may become important in future studies if other soluble substances, such as salts, are introduced as additional cloud components.

Equations 4 and 5 represent $N_B + 1$ ordinary differential equations. The solution for this system is obtained using the Analytical Predictor of Condensation (APC) scheme of Jacobson (1997b, 2002, 2005). The APC scheme conserves mass exactly and does not need iteration. Additionally, the scheme is numerically stable, as the gas concentration remains bounded between 0 and $C_{q,\text{tot}} = C_q + \sum_{i=1}^{N_B} c_{q,i}$ regardless of the time step.

Following the application of the APC scheme, the average volume for each bin is updated. All particle number density is transferred to the adjacent larger (or smaller) bin if the updated volume exceeds the upper (or falls below the lower) boundary of the current bin. When the particle size falls below (or exceeds) the minimum (or maximum) boundary of the size bin grid, the particle number density is recalculated using the smallest (or largest) radius of the size bin grid to ensure mass conservation.

2.4. Coagulation Scheme

We consider both self-coagulation within the same size distribution and heterogeneous coagulation between different types of size distributions. For example, coagulation within the CCN distribution results in the production of larger CCN particles and the depletion of smaller CCN particles. On the other hand, coagulation between CCN and pure sulfuric acid droplets leads to the production of larger mixed droplet particles and the depletion of smaller CCN and pure sulfuric acid droplets. The coagulation process is calculated using a volume-conserving semi-implicit scheme for any number N_T of size distributions, each with N_B bins, as follows (Jacobson, 2002, 2005).

$$c_{q,N_k,t+\Delta t} = \frac{c_{q,N_k,t} + \Delta t(T_{q,N_k,t+\Delta t,1} + T_{q,N_k,t+\Delta t,2})}{1 + \Delta t\, T_{q,N_k,t+\Delta t,3}} \tag{8}$$

Table 1
Coagulation Interaction in the Simulation

Type\Type	CCN distribution (A)	Sulfuric acid droplet distribution (B)	Mixed distribution (AB)
CCN distribution (A)	A	AB	AB
Sulfuric acid droplet distribution (B)	AB	B	AB
Mixed distribution (AB)	AB	AB	AB

Note. Each type represents a category of aerosol particles distinguished by their chemical composition or initial characteristics. For instance, the coagulation between CCN particles (Type A) and sulfuric acid droplets (Type B) results in the formation of mixed particles (Type AB), appearing in the first row and the second column in the table.

$$T_{q,N_k,t+\Delta t,1} = \sum_{M=1}^{N_T}\left[P_{N,M}\sum_{j=1}^{k}\left(n_{M_j,t}\sum_{i=1}^{k-1} f_{N_i,M_j,N_k,t}\cdot\beta_{N_i,M_j,t}\cdot c_{q,N_i,t}\right)\right] \tag{9}$$

$$T_{q,N_k,t+\Delta t,2} = \sum_{M=1}^{N_T}\sum_{I=1}^{N_T}\left[Q_{I,N,M}\sum_{j=1}^{k}\left(n_{M_j,t}\sum_{i=1}^{k} f_{I_i,M_j,N_k,t}\cdot\beta_{I_i,M_j,t}\cdot c_{q,I_i,t}\right)\right] \tag{10}$$

$$T_{q,N_k,t+\Delta t,3} = \sum_{M=1}^{N_T}\left[\sum_{j=1}^{N_B}\left[(1-L_{N,M})\left(1-f_{N_k,M_j,N_k,t}\right)+L_{N,M}\right]\beta_{N_k,M_j,t}\cdot c_{q,I_i,t}\right] \tag{11}$$

here, N_k is the index of the kth bin in the distribution N, Δt is the simulation time step, $\beta_{i,j}$ is the total coagulation kernel ($m^3\ s^{-1}$) between size bin i and j. Note that t and $t + \Delta t$ denote the current and advanced time steps, respectively.

The total coagulation kernel is the sum of contributions from Brownian diffusion and gravitational collection, with their formulations detailed in Pruppacher and Klett (1997). Particles formed through the coagulation process often fall between the sizes of adjacent bins. Therefore, partitioning between the adjacent bins is included for volume conservation, and this factor is represented by f_{i,M_j,N_k}, which is further expressed as follows (Jacobson et al., 1994).

$$V_{I_i,M_j} = v_{I_i} + v_{M_j} f_{I_i,M_j,N_k} = \begin{cases} \left(\dfrac{v_{N_k+1}-V_{I_i,M_j}}{v_{N_k+1}-v_{N_k}}\right)\dfrac{v_{N_k}}{V_{I_i,M_j}} & v_{N_k} \le V_{I_i,M_j} < v_{N_k+1} \quad k < N_B \\ 1-f_{I_i,M_j,N_k-1} & v_{N_k-1} < V_{I_i,M_j} < v_{N_k} \quad k > 1 \\ 1 & V_{I_i,M_j} \ge v_{N_k} \quad k = N_B \\ 0 & \text{all other cases} \end{cases} \tag{12}$$

The term T_1 given by Equation 9 accounts for the production of larger particles within distribution N from both self-coagulation ($N + N$) and heterogeneous coagulation involving distribution N (e.g., $N + M$). The term T_2 given by Equation 10 represents the production of particles in distribution N resulting from the heterogeneous coagulation of two distinct distributions (e.g., $I + M$). The term T_3 given by Equation 11 represents particle loss in distribution N due to both self-coagulation and heterogeneous coagulation.

The three size distributions assumed in this study interact with one another as summarized in Table 1. The parameters P, Q, and L account for interactions between different distributions. The CCN distribution consists of an involatile CCN material, while the sulfuric acid droplet distribution comprises a liquid binary mixture of H_2SO_4 and H_2O. Coagulation within each of these distributions produces larger particles within their respective distributions. In contrast, coagulation between these distributions leads to the formation of larger particles in the mixed distribution. Additionally, any coagulation involving the mixed distribution consistently results in larger particles within the mixed distribution.

Accordingly, the parameters P, Q, and L are defined based on these interactions. The parameter $P_{N,M}$ is set to 1 if particles in distribution N produce larger particles within the same distribution after coagulating with particles in

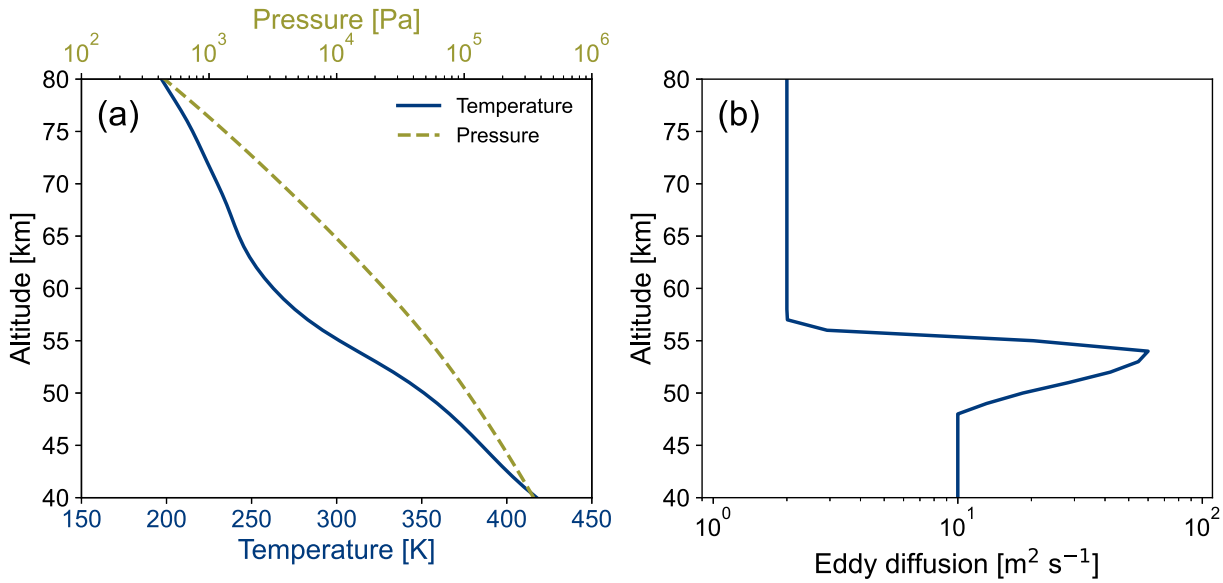

Figure 2. (a) Vertical profiles of temperature (blue solid line) and pressure (yellow dashed line) taken from Venus International Reference Atmosphere equatorial profiles (Seiff et al., 1985). (b) Vertical profile of the eddy diffusion coefficient from McGouldrick and Barth (2023).

distribution M, and 0 in all other cases. The parameter $Q_{I,M,N}$ is set to 1 if coagulation between particles in distributions I and M results in the formation of larger particles in distribution N, and 0 in all other cases. The parameter $L_{N,M}$ is set to 1 if particles in distribution N are removed from the distribution due to coagulation with particles in distribution M, and 0 in all other cases.

In the current framework, three types of particles are considered: CCN (Type A), H_2SO_4–H_2O droplets (Type B), and mixed droplets (Type AB), resulting in $N_T = 3$. Coagulation between particles within the same distribution produces larger particles within that distribution, and thus $P_{A,A}$, $P_{B,B}$, and $P_{AB,AB}$ are set to 1. When particles from different distributions coagulate, two scenarios are possible. In the first, a mixed particle coagulates with either a CCN particle or a sulfuric acid droplet to form a larger mixed particle; in this case, $P_{AB,A}$ or $P_{AB,B}$ is set to 1. In the second scenario, a CCN particle and a sulfuric acid droplet coagulate to form a new mixed particle, and $Q_{A,B,AB}$ is set to 1. For the corresponding loss processes, such as the coagulation of a CCN particle with a sulfuric acid droplet, both $L_{A,B}$ and $L_{B,A}$ are set to 1. This parameter is also set to 1 for homogeneous coagulation, so $L_{A,A}$, $L_{B,B}$, and $L_{AB,AB}$ are likewise all set to 1.

It should be noted that this framework can be applied to any number of distributions by setting up P, Q, and L based on the relationships between independent distributions. While extending the model to incorporate additional size distributions is beyond the scope of this paper, future research could utilize this framework to simulate the mixing of multiple aerosol types, providing a versatile tool for studying complex aerosol interactions.

2.5. Benchmark Simulations

The primary objective of this paper is to verify whether the algorithms described above function properly under Venusian atmospheric conditions. To achieve this, we perform both 0-D and 1-D simulations incorporating various processes. In the 0-D simulations, we begin with a simple system and gradually increase the complexity to ensure that the microphysical scheme operates as expected. The background atmospheric temperature and pressure are set to the equatorial profiles of the Venus International Reference Atmosphere (VIRA) (Seiff et al., 1985) for both 0-D and 1-D simulations, as shown in Figure 2a.

The first phase of the 0-D simulations focuses exclusively on particle growth through condensation and evaporation. The results obtained using the moving-center scheme are validated against those of exact solutions calculated with the full-moving scheme. The second phase explores various scenarios involving both growth and coagulation processes to verify the algorithm's capability to simulate aerosol microphysics across a wide range of complexities.

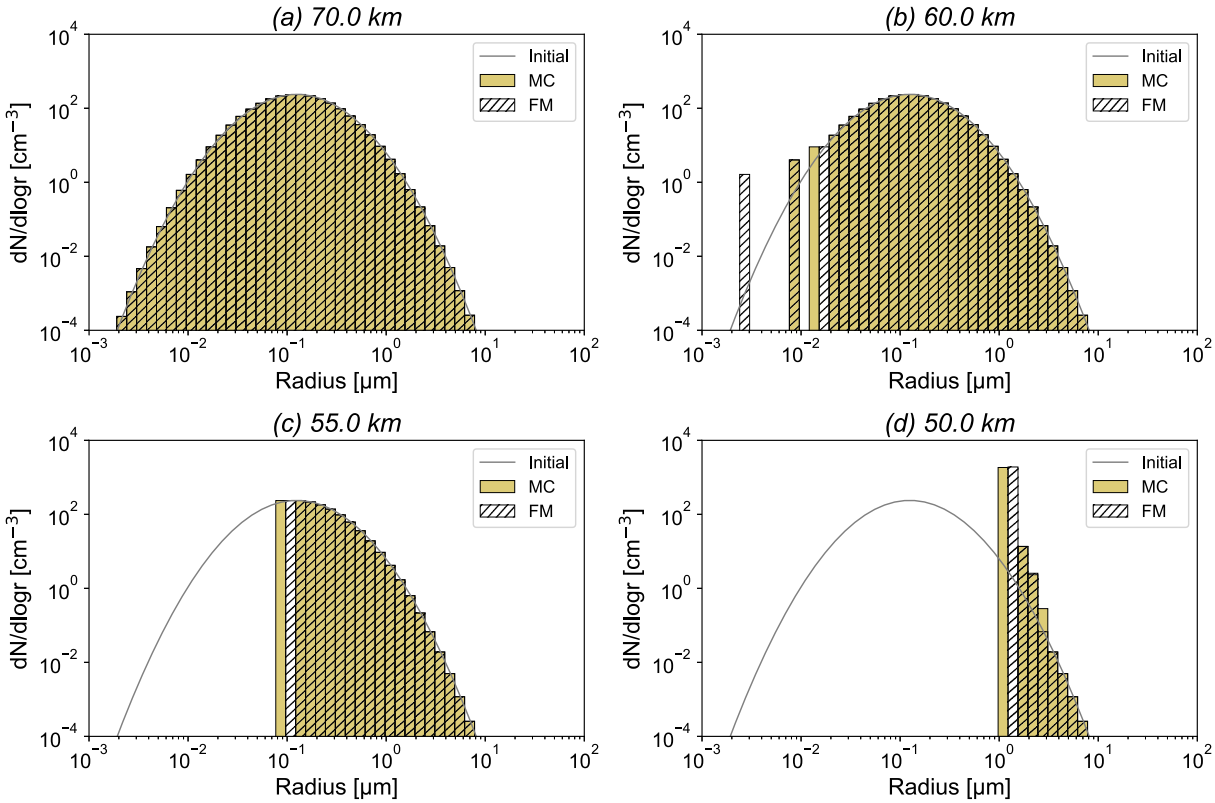

Figure 3. Comparison of the moving-center (MC: yellow fill) and full-moving (FM: hatched fill) schemes for H_2SO_4 vapor growth onto aerosol particles at altitudes of panel (a) 70 km, (b) 60 km, (c) 55 km, and (d) 50 km. The initial size distribution is plotted with a dotted line.

Two benchmark 1-D simulations are performed to validate our model, including transport processes. In the first benchmark case, we validate SPECK against an existing model that utilizes the full-stationary scheme. The model of K2024 serves as a proxy for a full-stationary microphysics model. In the second benchmark case, we perform 1-D simulations under the same settings as McGouldrick and Barth (2023), demonstrating a realistic application of our model to the Venusian cloud system. The eddy diffusion coefficient is set to the same value in the first and second benchmark cases, and these values are taken from McGouldrick and Barth (2023). The profile has a peak value of 60 $m^2\ s^{-1}$ at 54 km altitude, a constant value of 2 $m^2\ s^{-1}$ above 57 km altitude, and 10 $m^2\ s^{-1}$ below 48 km altitude (Figure 2b). The full profile is given in Figure 2b.

3. 0-D Validation of the Moving-Center Scheme

3.1. Condensation Alone

We performed a 0-D model experiment to validate the newly introduced condensation scheme using the moving-center scheme. This simulation considers only condensation and evaporation processes, with H_2SO_4 as the sole condensational species for simplicity. The initial conditions include a log-normal size distribution of H_2SO_4 particles corresponding to Mode 1, with 5% supersaturation of H_2SO_4 vapor. The total number of H_2SO_4 in liquid and gas phases remains constant since no chemical production or flux outside of the box is considered. In addition to the moving-center scheme, we performed simulations under the same conditions using the full-moving scheme, which provides an exact solution for condensational growth. The time step was set to 10 s, and the 0-D simulations were run for 1,000 s at four different atmospheric conditions corresponding to altitudes of 70, 60, 55, and 50 km, as shown in Figure 2a.

The moving-center results are in good agreement with those of the full-moving scheme (Figure 3). The system rapidly reaches a near steady-state condition where the ambient vapor pressure equilibrates close to the saturation vapor pressure. Under such conditions, the saturation ratio becomes size-dependent due to the Kelvin effect,

Table 2
The Normalized Relative Error of the Total Number Density and Mean Radius of the Moving-Center Scheme Relative to the Full-Moving Scheme

Altitude (km)	Total number density error (%)	Mean radius error (%)
70	0	0
60	11.2	0.3
55	14.8	13.7
50	3.1	11.1

which raises the effective saturation vapor pressure over smaller particles. In addition, the rate of change in their volume is much slower for larger particles due to their lower surface-area-to-volume ratio. As a result, small particles experience evaporation, while larger particles are in a state of growth or near-equilibrium.

At 70 km altitude, the results are identical because the condensational mass flux is not significant at this altitude due to the low H_2SO_4 vapor number density of 5.1×10^{12} m^{-3}. Condensation and evaporation significantly affect the size distribution at 60, 55, and 50 km where the H_2SO_4 vapor number densities are 2.4×10^{15}, 5.3×10^{17}, and 5.4×10^{19} m^{-3}, respectively. Evaporation of smaller particles is observed at 60 and 55 km, with slight differences in the timing of evaporation between the two schemes. At 50 km altitude, the effects of growth are more pronounced than at higher altitudes, due to the increased availability of H_2SO_4 vapor under high-temperature conditions. A pit structure forms between 1 and 2 μm as a result of rapid condensational growth. However, despite the formation of the pit, the results from both methods closely align.

We calculated the normalized relative error of the moving-center scheme relative to the full-moving scheme at the end of the simulation (Table 2). The largest error in total number density is 14.8% at 55 km altitude, while the largest error in mean radius is 13.7%, also at 55 km altitude. The mean radius error obtained here is consistent with the 12% error reported in a previous microphysics algorithm comparison study (Zhang et al., 1999). They also demonstrated that the moving-center scheme yields lower errors than other schemes used in Earth's air-quality models and concluded that the moving-center scheme performs best for condensation. This consistency with previous research strengthens the reliability of the moving-center scheme, especially under conditions relevant to cloud condensation processes.

Figure 4 shows the time series of the particle size distribution at various altitudes. Evaporation occurs at 60 and 55 km altitudes, causing particles at the lower edge of the distribution to shift into smaller size bins. The evaporating particles remain within a single size bin, demonstrating that the moving-center scheme effectively eliminates numerical diffusion. In contrast, Toon et al. (1988) reported that with the full-stationary scheme, the size distribution broadens over time and diverges from the exact solution due to numerical diffusion, particularly when the evaporation rate is rapid. This contrast highlights the benefits of the moving-center scheme, which preserves the integrity of the particle size distribution during rapid evaporation.

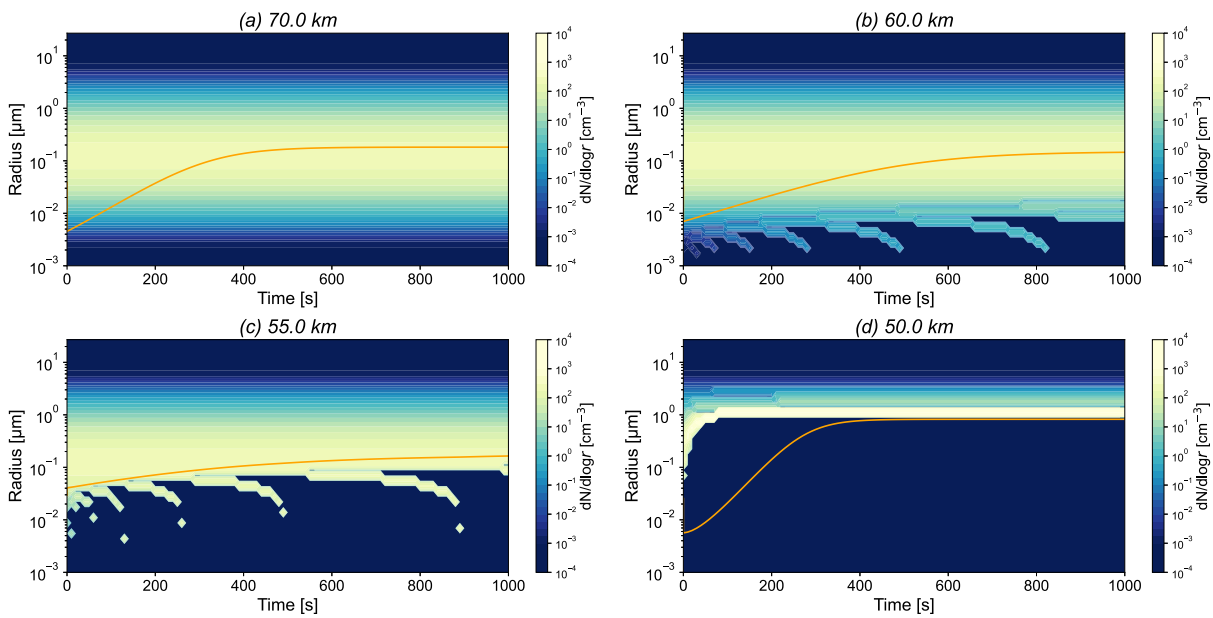

Figure 4. Aerosol size distribution as a function of time and radius at altitudes of panel (a) 70 km, (b) 60 km, (c) 55 km, and (d) 50 km, plotted with critical radius determined by saturation vapor pressure (orange line). The downward (upward) shift of the size distribution corresponds to evaporation (condensation).

On the other hand, given that real atmospheric size distributions are continuous rather than discrete, it may be questionable whether evaporation in nature occurs through such intermittent migrations of isolated size modes toward smaller radii. To examine this, we conducted additional simulations with higher bin resolution (Figure S1 in Supporting Information S1). These simulation runs demonstrated that particle evaporation proceeds in a more gradual and continuous manner as the resolution increases, consistent with expectations for natural systems. This confirms that the intermittent bin migration observed in the original figure was a resolution artifact, rather than a result of inaccurate evaporation treatment in the model.

The evolution of the critical radius provides further insight into how the particle size distribution is influenced by ambient saturation vapor pressure. The critical radius r_c is determined as:

$$r_c = \frac{2\sigma_p m_w}{RT\rho_w \ln S_q} \tag{13}$$

where S_q is the supersaturation of the condensing vapor. The critical radius refers to the specific size that a particle must reach in order to continue growing spontaneously. At the beginning of the simulation, high ambient H_2SO_4 vapor pressure results in high supersaturation and a correspondingly small critical radius. As larger particles grow via condensation, they deplete the vapor concentration, leading to a gradual increase in the critical radius. This shift impacts the particle size distribution differently across altitudes due to variations in saturation vapor pressure. At 50 and 55 km, the system responds relatively quickly, and the lower edge of the size distribution closely tracks the critical radius. This behavior is driven by strong condensation and evaporation fluxes associated with high H_2SO_4 saturation vapor pressure. In contrast, at higher altitudes, such as 60 and 70 km, where vapor pressure is lower, the response is significantly slower. In particular, the radial growth rate is less than 1 nm hr^{-1} for a particle with a radius of 0.01 μm, resulting in no observable changes to the particle size distribution over the simulation timescale.

The pit structure can serve as an indicator of condensation and evaporation. In Figure 4b, continuous evaporation occurs around 0.01 μm, causing the size bins to shift toward smaller radii. As the number density in one bin shifts, a pit structure forms in the bin that originally preserved the number density. Subsequently, the number density from the neighboring bin moves to fill the pit. As a result, the pit structure appears to shift toward larger radii during continuous evaporation in a smooth size distribution. On the other hand, rapid condensational growth occurs during the first 200 s at 50 km altitude (Figure 4d). In this case, the number density distribution shifts toward larger radii. The pit structure created by this process is then replenished by the number density from smaller bins. As a result, the pit structure appears to shift toward smaller radii during condensation growth.

In 0-D box simulations, repeated condensation and evaporation in the moving-center scheme can lead to a narrowing of the aerosol size distribution over time through pit formation, potentially concentrating particles into fewer bins. However, in realistic simulations, such repeated narrowing does not typically occur for the following reasons. First, there are continuous aerosol sources and sinks–such as nucleation, emissions, and photochemical production–that help maintain a broad size distribution. Second, multi-dimensional mixing effectively smooths out the pit structures that are more prominent in 0-D models (Mohs & Bowman, 2011). Furthermore, the choice of appropriate bin spacing and resolution further mitigates excessive narrowing. Due to these reasons, many models have successfully implemented moving-center schemes in Earth studies (e.g., Bergman et al., 2012; Fast et al., 2006; Jacobson et al., 2007; Mann et al., 2012; Matsui, 2017), and its applicability to the Venusian atmosphere in 1-D is carefully tested in Section 4.

3.2. Condensation and Coagulation

Next, we performed a 0-D simulation including both condensation and coagulation processes. All processes described in Section 2 are incorporated, except for transport, chemical production of H_2SO_4 and CCN, and chemical loss of H_2O. This model considers three particle distributions consisting of CCN, sulfuric acid droplets, and a mixture of CCN and sulfuric acid droplets. The initial particle distribution consists of an excessive number of Mode 1 particles with a smaller mean radius and Mode 2 particles, as shown in Figure 5a. Mode 1 particles consist of CCN, while Mode 2 particles consist of sulfuric acid droplets. This simulation is analogous to the numerical experiment conducted by Knollenberg and Hunten (1980), but it introduces a Mode 2 particle

10.1029/2025EA004203

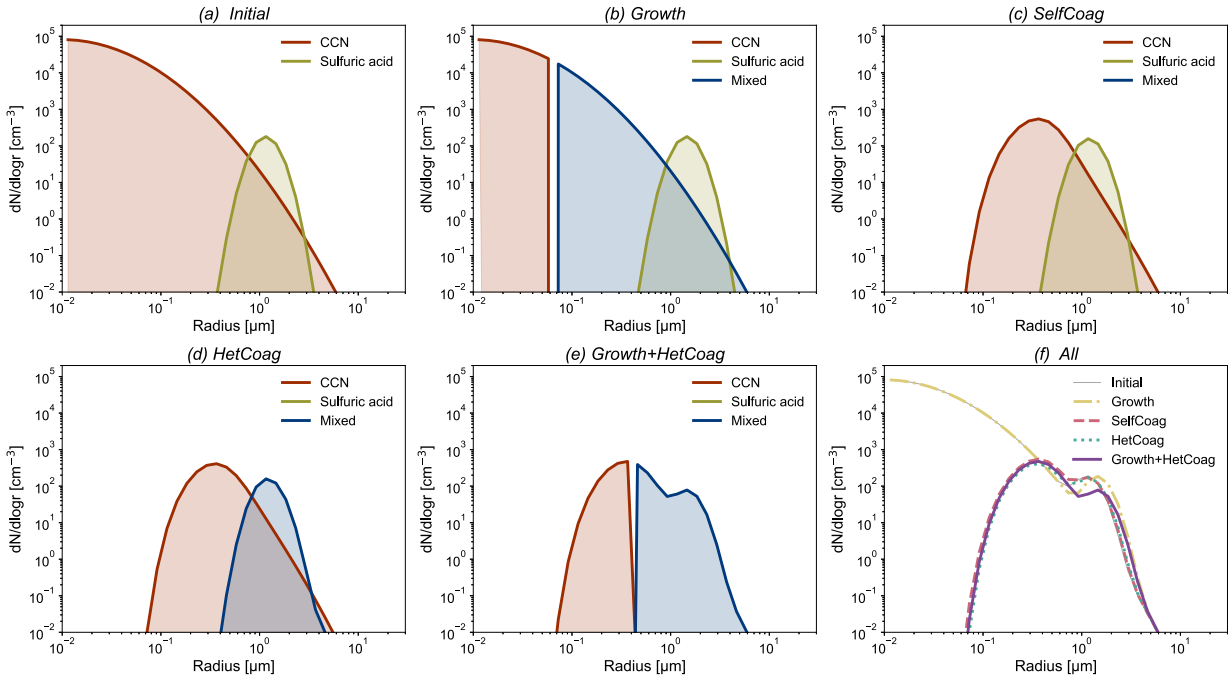

Figure 5. Size distributions of Cloud Condensation Nucleus (red line), sulfuric acid droplet (yellow line), and mixed (blue line) particles at panel (a) the beginning of the simulation and at the end of simulations with (b) growth alone, (c) self-coagulation alone, (d) heterogeneous coagulation alone, (e) combined growth and heterogeneous coagulation, and (f) a comparison of panels (a) to (e).

distribution with a mode radius of 1.16 μm to observe particle interactions between independent distributions. Atmospheric temperature and pressure were taken from 60 km altitude in the VIRA profile (Figure 2a). The simulation was run for 60 Earth days, following Knollenberg and Hunten (1980). The initial conditions for the condensable species were set to 5% supersaturation for H_2SO_4 and 30 ppm for H_2O. We performed a series of simulations considering different processes: growth alone, self-coagulation alone, heterogeneous coagulation alone, and the combination of condensational growth and heterogeneous coagulation.

The results confirm that the algorithm effectively captures a wide range of particle interaction scenarios. In the growth-only simulation (Figure 5b), CCN particles larger than 0.05 μm are activated and join the mixed size distribution, while sulfuric acid droplets grow slightly from a mode radius of 1.16–1.47 μm but remain outside the mixed distribution. In the self-coagulation-only experiment (Figure 5c), the smaller tail of the Mode 1 distribution significantly decreases due to coagulation, consistent with the numerical experiment by Knollenberg and Hunten (1980). The heterogeneous-coagulation-only experiment shows a similar profile for Mode 1 and Mode 2 particles as observed in the self-coagulation-only case (Figure 5d). However, in this scenario, the Mode 2 particles transition into the mixed particle distribution due to heterogeneous coagulation between the CCN and sulfuric acid droplet distributions. By the end of the simulation, almost all sulfuric acid droplets have been converted into mixed particles.

When both growth and heterogeneous coagulation are considered, scavenging of Mode 1 particles, a shift in the mode radius of Mode 2 particles from 1.16 to 1.47 μm, and aerosol mixing are observed (Figure 5e). This can be interpreted as a combined effect of the growth-only and heterogeneous-coagulation-only experiments. These results indicate that the algorithm effectively captures the complex interactions between growth, coagulation, and mixing processes.

4. 1-D Simulations

4.1. Benchmark Simulation I: Comparison With the Full-Stationary Scheme

In the first benchmark case, we used the K2024 model as a proxy for the full-stationary scheme and validated SPECK against the existing model. The K2024 model contains a single size distribution consisting of the H_2SO_4-

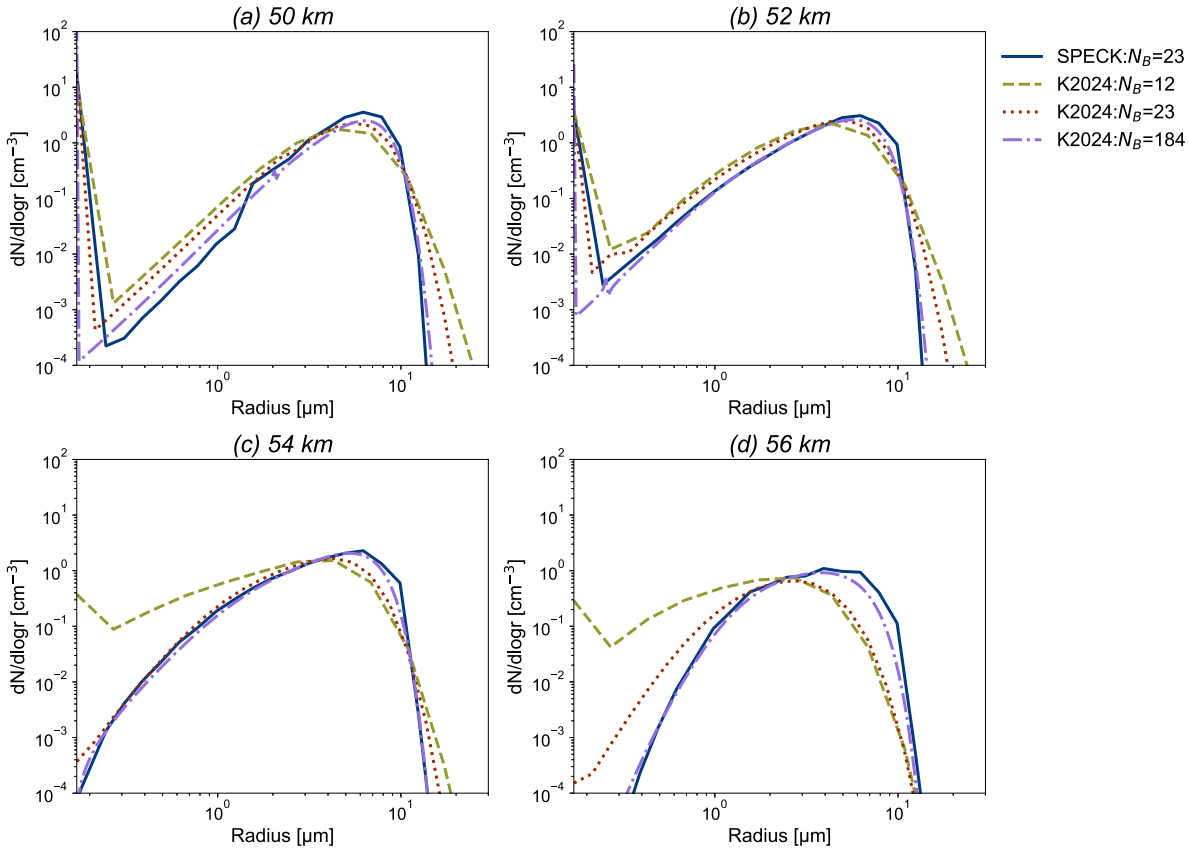

Figure 6. Steady-state size distribution at various altitudes calculated by SPECK (blue solid line) and K2024 model with different bin resolutions plotted with yellow dashed line ($N_B = 12$), red dotted line ($N_B = 23$), and purple dot-dashed line ($N_B = 184$). Note that the resolution of SPECK is $N_B = 23$.

H_2O solution and CCN material, and hence, the mixing between multi-distributions is not calculated. This simple configuration is also adopted in SPECK for this benchmark case. The size bin ranges from 0.17 to 30 μm, and the resolution is varied from low resolution ($V_{rat} = 4$; $N_B = 12$) to high resolution ($V_{rat} = \sqrt[8]{2}$; $N_B = 184$) to evaluate the resolution dependence of the moving-center and full-stationary schemes. The simulations are performed under the same conditions.

The model domain extends from 40 to 60 km with a vertical step of 1 km. Photochemical production of H_2SO_4 vapor and CCN material is excluded for simplicity. The lower boundary conditions for H_2SO_4 and H_2O are set to 10 and 30 ppm at 40 km, respectively. The CCN particle density at the lower boundary is represented by a monodisperse distribution of the smallest particles (0.17 μm) with the particle number density of 40 cm^{-3}, following K2024. At the upper boundary, zero fluxes are assumed for both vapors and particles. The initial condition of all vertical levels is a uniform distribution, set to the value of the lower boundary for vapor and particle species. The timestep is set to 10 s, and the simulation is run for 10^8 s, which is sufficiently longer than the time needed to reach steady state. The simulation results are averaged over the last 10^6 s to compare with the steady-state results obtained by the K2024 model.

Figure 6 presents the size distribution at various altitudes for SPECK and the K2024 model with different bin resolutions. In the K2024 results, size distributions tend to broaden at all altitudes when bin resolution is coarse. This broadening effect is particularly evident in smaller size bins at altitudes of 54 and 56 km at the lowest bin resolution. Additionally, the upper edge of the size distribution also exhibits broadening, especially at 50, 52, and 54 km. As the bin resolution becomes finer, the size distribution narrows. In contrast, SPECK results show less broadening compared to the K2024 model with the same bin resolution ($N_B = 23$). Furthermore, as the bin resolution of the K2024 model increases, its results converge toward those of SPECK.

10.1029/2025EA004203

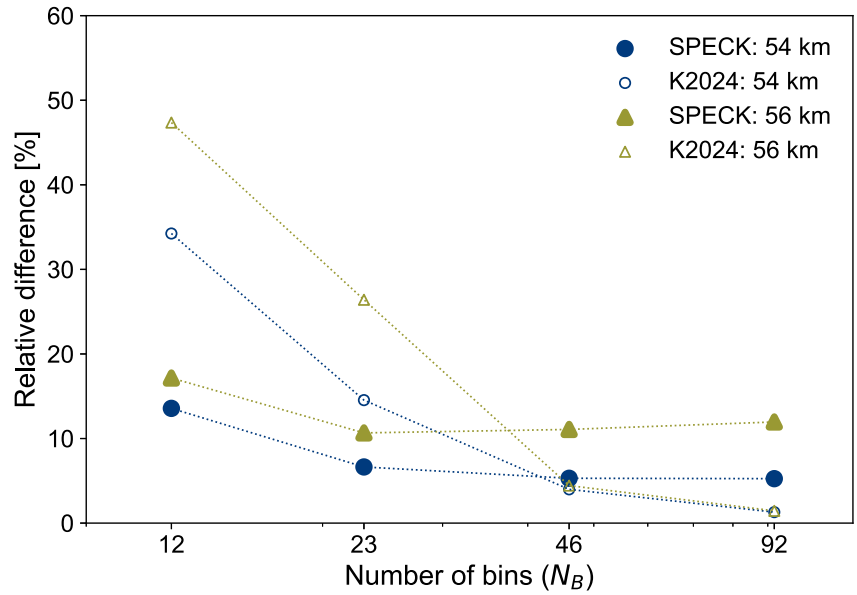

Figure 7. Relative differences (%) in the mean radius simulated by SPECK and the K2024 model compared to a reference value at various altitudes as a function of the number of bins. The result of the highest resolution of the K2024 model ($N_B = 184$) is used as a reference value. The four data points at each altitude represent $N_B = 12, 23, 46,$ and 92.

The close agreement between SPECK and the high-resolution full-stationary scheme highlights the resilience of the moving-center scheme against numerical diffusion. In the full-stationary scheme implemented in K2024, numerical diffusion occurs at lower bin resolutions because size growth is represented as Eulerian advection in size space. Generally, numerical diffusion effects diminish as resolution increases relative to the scale of the physical process, allowing fine structures to be resolved. This trend is evident in Figure 6, where the size distribution narrows with increasing resolution. In contrast, the moving-center scheme implemented in SPECK nearly eliminates numerical diffusion by calculating growth using a Lagrangian approach. As a result, the predicted size distribution does not exhibit broadening and closely matches the results of the high-resolution full-stationary scheme. This demonstrates that SPECK can achieve size distribution predictions comparable to high-resolution full-stationary simulations without requiring fine bin resolution.

It should be noted that the SPECK particle number density at 50 km exhibits a rapid decrease around a 1.5 μm radius (Figure 6a), which is attributed to the Lagrangian treatment of evaporation. Near the cloud bottom at 50 km, the evaporation timescale is extremely short, and this process is observed as Lagrangian advection of a single size bin toward smaller radii, as illustrated in Figure 4c. Consequently, after time averaging, the size distribution at 50 km appears discontinuous around 1.5 μm, below which particle evaporation dominates. This method of evaporation aligns with the exact solution, as demonstrated in Figure 3, and reflects the behavior of real atmospheric processes. In contrast, the K2024 results predict a smooth decrease in number density toward smaller radii. This feature arises from the Eulerian treatment of evaporation, where the scheme handles evaporation through the number density flux between adjacent size bins. As a result, the Eulerian scheme causes particle number density to spread across size bins where particles should not exist, creating a smoother but less physically accurate size distribution.

Figure 7 shows the relative differences in the mean radius simulated by SPECK and the K2024 model compared to reference values. The reference value is chosen as the mean radius calculated by the highest resolution ($N_B = 184$) of K2024, serving as the "true" value. The results from the K2024 model with lower resolutions converge toward the reference value as resolution increases, a trend also observed in Figure 6. The relative difference for the K2024 model decreases by nearly half as the resolution is doubled, reflecting the reduced impact of numerical diffusion with increasing resolution.

In contrast, the relative difference for SPECK remains consistent across various bin resolutions. Specifically, for bin resolutions greater than $N_B = 23$, the values are very similar, with differences of <15% at 56 km and <8% at

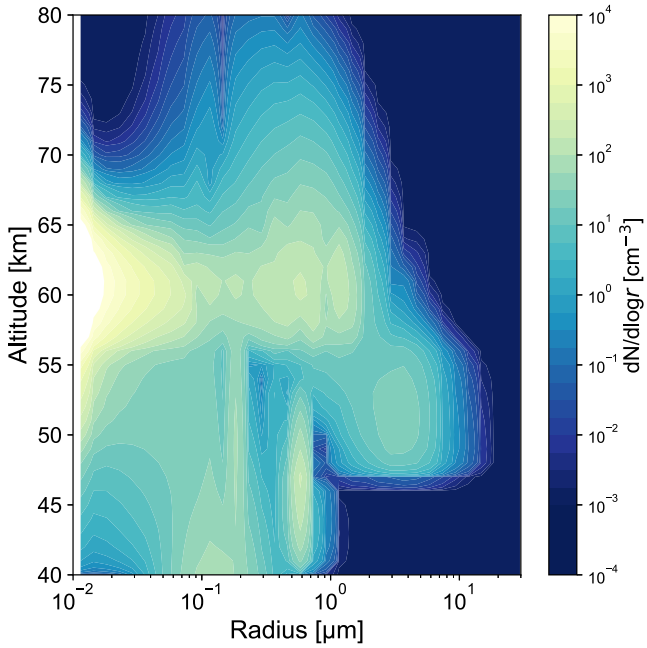

Figure 8. Combined size distribution of Cloud Condensation Nucleus and mixed particles as a function of particle radius and altitude in the nominal resolution case ($V_{rat} = 2$).

54 km. This consistency is due to the resilience of the moving-center bin scheme against numerical diffusion. As a result, SPECK predicts a mean radius more accurately than the K2024 model when the bin resolution is lower than $N_B = 46$. A typical resolution used in microphysics models is $V_{rat} = 2$, which indicates that the particle volume doubles between adjacent bins, as indicated by Equation 4. The resolution corresponds to $N_B = 23$ in this simulation. As shown in Figure 7, SPECK achieves closer agreement with the reference value compared to the K2024 model at this typical resolution, highlighting enhanced performance in typical microphysics simulation settings.

4.2. Benchmark Simulation II: Comparison With McGouldrick and Barth (2023)

In the second benchmark case, we perform 1-D simulations with the same setting as the recent Venus microphysics study by CARMA (McGouldrick & Barth, 2023). This simulation serves as a realistic application of our model to the Venusian cloud system. Two types of simulations were conducted, varying the size bin resolution from nominal ($V_{rat} = 2$) to low ($V_{rat} = 4$) resolution cases, with size bins ranging from 10 nm to 30 μm. The former has the same resolution as CARMA, while the latter has a resolution that is half that of CARMA.

The model spans from 40 to 80 km with a vertical grid step of 1 km and considers two types of size distributions consisting of CCN and mixed particles. In addition to self-coagulation, heterogeneous coagulation between the two distributions is included. The chemical production of H_2SO_4 vapor is represented by a Gaussian distribution with a column production rate of 6×10^{15} m^{-2} s^{-1}, representing $\left[\frac{\partial C_q}{\partial t}\right]_{chem}$ in Equation 4 for $q = 1$. The peak altitude and half width of the Gaussian distribution are 61 and 2 km, respectively. The loss of H_2O and production of elemental sulfur S is scaled by the following net chemical reaction (Imamura & Hashimoto, 2001).

$$2H_2O + 3SO_2 \rightarrow 2H_2SO_4 + S \quad (14)$$

This reaction results in the loss of two H_2O molecules and the production of one S atom per production of two H_2SO_4 molecules. The lower boundary conditions for H_2SO_4 and H_2O are set to 10 and 30 ppm at 40 km, respectively. The concentrations of these gas species are assumed to be zero above the upper boundary. The population of CCN particles is fixed to a lognormal distribution at the lower boundary following the LCPS observation by Knollenberg and Hunten (1980), while liquid components are assumed to be zero. The upper boundary conditions of all particles are set to zero flux. We refer the reader to McGouldrick and Barth (2023) for more detailed descriptions of the model and settings.

We set the timestep to 10 s and ran the simulation for 10^8 s, which is sufficiently longer than the timescales of the physical processes incorporated within the model, such as eddy diffusion, sedimentation, condensation, and coagulation. We confirmed that the pit formation does not increase in severity as the simulation progresses (Figures S1–S5 in Supporting Information S1). Simulation results are averaged over the last 10^6 s of the simulation for comparison with the steady-state results obtained by McGouldrick and Barth (2023).

Figure 8 shows the simulated size distribution as a function of particle radius and altitude, and Figure 9 shows the size distribution at various altitudes in the nominal resolution case ($V_{rat} = 2$). The cloud structure can be divided into two distinct layers: a condensational cloud below 57 km and a photochemical cloud above 57 km. The former corresponds to the lower and middle cloud layers observed by the LCPS (Knollenberg & Hunten, 1980), while the latter corresponds to the upper cloud and upper haze. Larger particles, ranging from 1 to 10 μm, are evident in the condensational cloud, corresponding to Mode 2 and Mode 3 particles (Figures 9c and 9d). These cloud particles form as a result of vigorous condensation driven by the enhanced eddy diffusion. In addition to the larger particles, there is also a small particle population with radii smaller than 1 μm. This population is composed mainly of

10.1029/2025EA004203

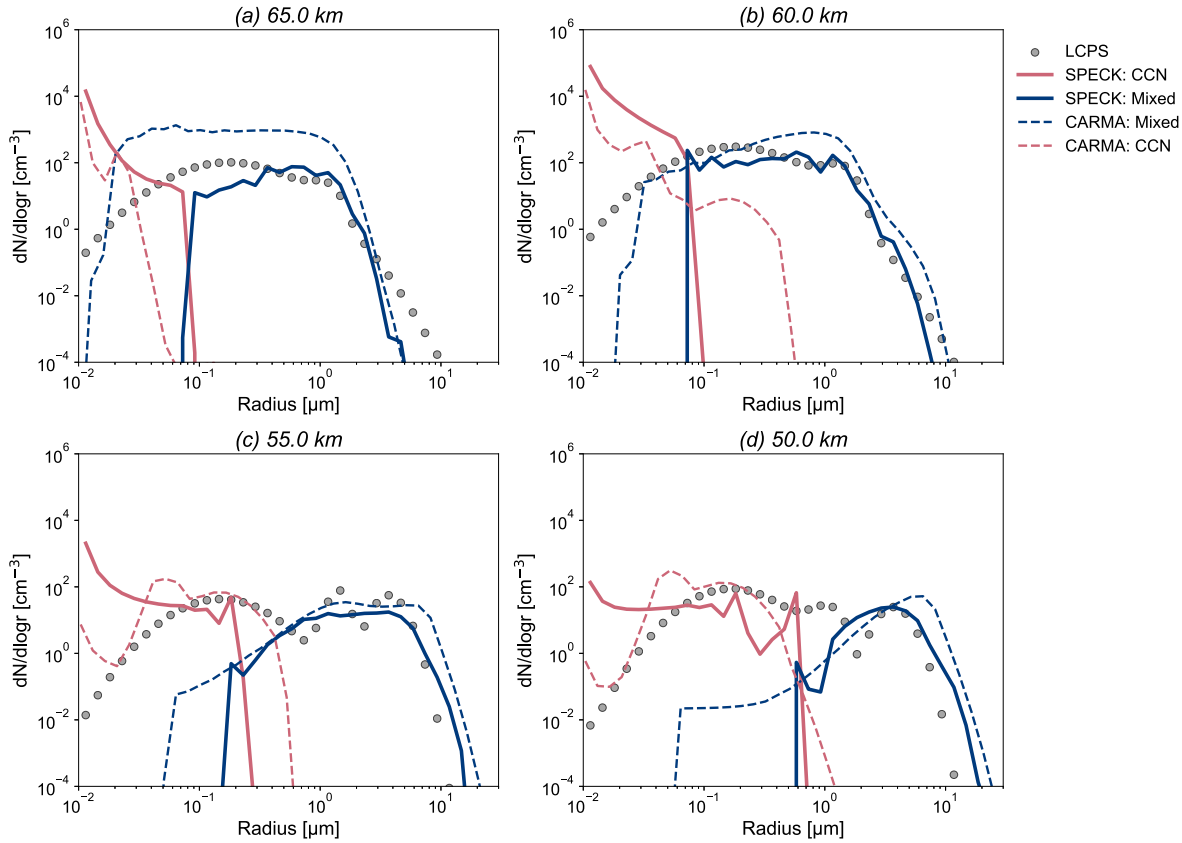

Figure 9. Size distribution of the Cloud Condensation Nucleus (red solid line) and Mixed particles (blue solid line) at altitudes of panel (a) 65 km, (b) 60 km, (c) 55 km, and (e) 50 km in the nominal bin resolution case (V_{rat} = 2). Equatorial profiles from the CARMA simulation (McGouldrick & Barth, 2023) also plotted with dashed lines. The simulated distributions are compared with the LCPS in situ measurements by Knollenberg and Hunten (1980) (gray circles).

CCN particles. The CCN particles remain unwetted because their radii are smaller than the critical radius defined by the Kelvin effect.

Above the condensational cloud lies the photochemical cloud, which is maintained through the chemical production of H_2SO_4 vapor. The most populated region is around 0.01 μm due to the photochemical production of CCN particles (Figures 9a and 9b). These CCN particles grow to approximately 0.1 μm by coagulation, where they overcome the Kelvin barrier and join the mixed droplet size distribution. These droplets grow by condensation and join the condensational cloud through sedimentation, while some particles are carried upward by eddy diffusion and contribute to the upper haze above 70 km. The structure and particle cycles are similar to those described by McGouldrick and Barth (2023), indicating that our model successfully captures the general characteristics of the Venusian cloud layers.

The simulated CCN distributions exhibit two distinct peaks below 57 km, as shown in Figures 8, 9c, and 9d. These two peaks originate from different altitudes. The peak around 0.6 μm forms when mixed particles evaporate near the cloud base, leaving behind their CCN. A similar peak is observed in the CCN distribution from CARMA, although the peak radius is somewhat smaller around 0.05 μm. In contrast, the peak around 0.2 μm is generated by the evaporation of mixed particles descending from the upper cloud.

The upper cloud region is highly supersaturated with H_2SO_4 vapor, which minimizes the impact of the Kelvin effect. However, when these particles enter the less supersaturated middle cloud, the Kelvin effect becomes significant, causing particles smaller than the critical radius to evaporate. These peaks may be better resolved than in the previous study due to the use of the moving-center bin scheme. As shown in Figure 4, the moving-center scheme allows size bins to evaporate to their exact sizes while minimizing numerical diffusion.

10.1029/2025EA004203

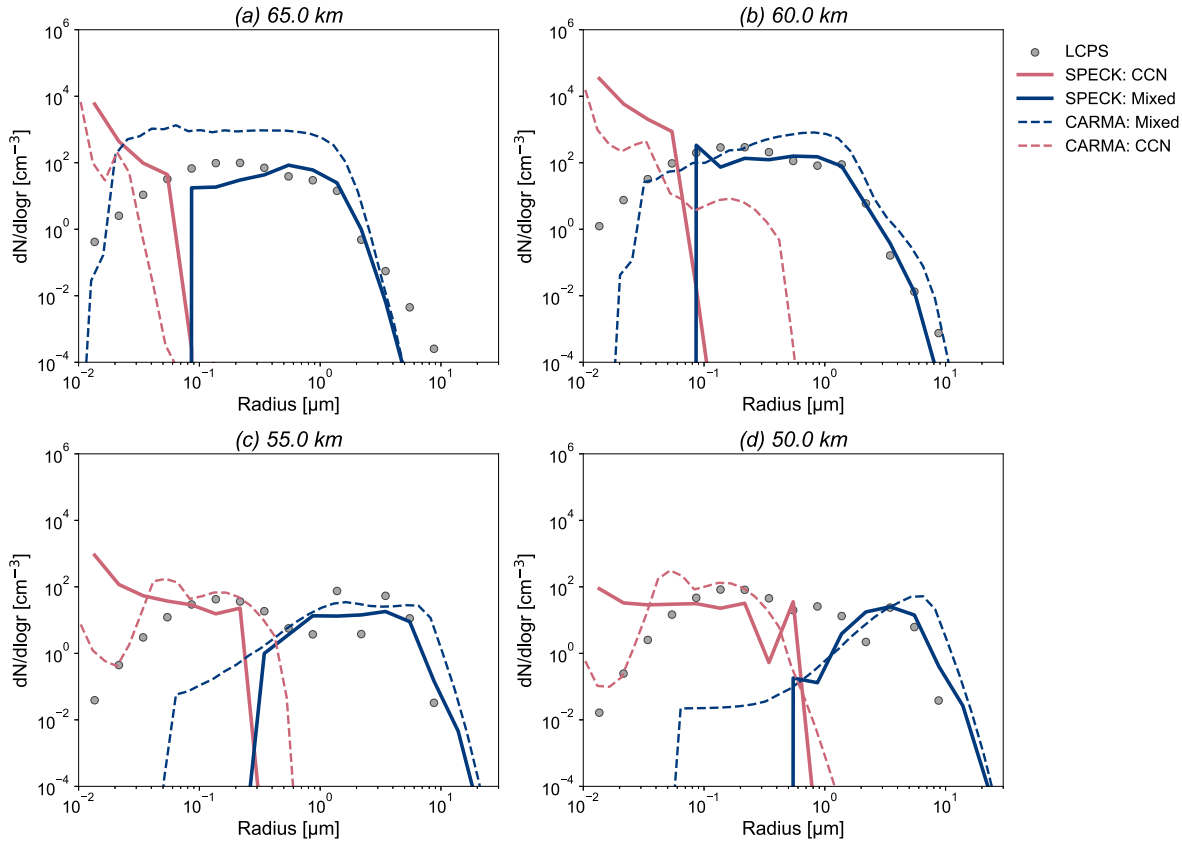

Figure 10. Size distribution of the Cloud Condensation Nucleus (red solid line) and Mixed particles (blue solid line) at altitudes of panel (a) 65 km, (b) 60 km, (c) 55 km, and (e) 50 km in the low bin resolution case ($V_{\text{rat}} = 4$). Equatorial profiles from the CARMA simulation (McGouldrick & Barth, 2023) also plotted with dashed lines. The simulated distributions are compared with the LCPS in situ measurements by Knollenberg and Hunten (1980) (gray circles).

Consequently, the CCN distribution remains confined to a very narrow region without spreading when it is left behind by evaporation.

Figure 10 shows the size distribution at various altitudes in the low resolution case ($V_{\text{rat}} = 4$). The simulated distributions are nearly identical to those simulated with nominal bin resolution (Figure 9). As already seen in Section 4.1, the moving-center scheme predicts similar size distributions regardless of the bin resolution, and this trend is reproduced under more complex settings.

In the current simulation settings, halving the bin resolution reduced the computation time to about 0.16 times that of the nominal resolution, yielding a sixfold efficiency gain. This efficiency is especially critical for 3-D modeling, as fewer size bins lower both the number of tracers and the computational load, making explicit microphysics calculations more feasible. In existing 3-D Venus cloud simulations, microphysics processes are not explicitly calculated, and cloud sizes are represented by three separate modes (Stolzenbach et al., 2023) or four modes (Karyu et al., 2023). The results from SPECK suggest that the number of size bins needed to reasonably simulate microphysical properties can be as low as $N_B = 12$, only three to four times larger than the number of cloud modes currently used in the 3-D models.

Implementing the moving-center scheme in GCMs provides additional advantages that offset the computational cost. By reducing numerical diffusion and accurately representing size distributions with fewer bins, this scheme enables more precise cloud microphysics simulations. This is crucial for understanding cloud dynamics, particle cycling, and radiative effects in Venus's atmosphere. Overall, the moving-center scheme offers an efficient and practical path to incorporating full microphysics in 3-D models, potentially enhancing the predictive capability of Venus GCMs.

5. Conclusions and Future Prospects

We presented a new microphysics model based on the moving-center bin scheme, which effectively eliminates numerical diffusion caused by condensation and evaporation processes. The model also includes interactions between multiple size distributions, making it more versatile for simulating the composition and mixing state of aerosols.

The 0-D simulation results confirm that the microphysics framework is a robust and reliable tool for modeling aerosol microphysics on Venus, particularly in capturing condensation and evaporation dynamics. The 0-D simulation using condensation alone showed nearly identical results with the exact solution with a normalized relative error of less than 15%. Heterogeneous coagulation processes significantly change the composition of aerosols, highlighting the importance of mixing between independent size distributions.

We performed two benchmark simulations to validate SPECK against existing models. In the first benchmark case, we compared our simulation results to those computed using a full-stationary bin scheme (K2024) with varying bin resolutions. We found that SPECK can predict size distributions similar to those obtained with the high-resolution full-stationary scheme, regardless of the bin resolution. In contrast, the size distributions predicted by the K2024 model strongly depend on bin resolution and deviate from the high-resolution results as the resolution decreases. This demonstrates that SPECK successfully eliminates the effects of numerical diffusion, highlighting its capability for high-accuracy condensation modeling.

In the second benchmark case, we further validated SPECK by comparing our results to those from recent 1-D simulations using CARMA (McGouldrick & Barth, 2023), applying the same simulation settings. The simulated size distributions are in good agreement with CARMA and in situ LCPS observations, indicating that SPECK can accurately reproduce the complex cloud structure of Venus. Additionally, a simulation performed at lower resolution produced consistent results, demonstrating that SPECK can simulate Venusian cloud microphysics accurately without requiring a large number of bins. Notably, reducing the bin resolution by half resulted in an efficiency increase of more than six times compared to the original, while maintaining simulation accuracy. These findings suggest that SPECK is both efficient and well-suited for future 3-D modeling applications.

Future work can build on this framework to model multi-distribution interactions with high accuracy, offering further insights into complex aerosol processes in the Venusian atmosphere. This framework is also applicable to various planetary atmospheres with aerosols, including Mars, Titan, the gas giants, and exoplanets.

Data Availability Statement

The SPECK source code and the simulation outputs used to produce the results presented in this paper are accessible via Karyu (2025).

Acknowledgments
This study was supported by the Japan Society for the Promotion of Science (JSPS) (KAKENHI Grants JP22H00164, JP23KJ0201, JP23K25932, and JP24K21561), JST FOREST Program (Grant JPMJFR212U, Japan), and the International Joint Graduate Program in Earth and Environmental Sciences (GP-EES) of Tohoku University. We thank two anonymous reviewers for helpful comments.

References

Bergman, T., Kerminen, V.-M., Korhonen, H., Lehtinen, K. J., Makkonen, R., Arola, A., et al. (2012). Evaluation of the sectional aerosol microphysics module SALSA implementation in ECHAM5-HAM aerosol-climate model. *Geoscientific Model Development*, *5*(3), 845–868. https://doi.org/10.5194/gmd-5-845-2012

Chaffin, M. S., Cangi, E. M., Gregory, B. S., Yelle, R. V., Deighan, J., Elliott, R. D., & Gröller, H. (2024). Venus water loss is dominated by HCO+ dissociative recombination. *Nature*, *629*(8011), 1–4. https://doi.org/10.1038/s41586-024-07261-y

Eisenberg, D., & Kauzmann, W. (1969). *The structure and properties of water*. Oxford University Press.

ESA. (2023). EnVision, understanding why Earth's closest neighbour is so different, Definition Study Report (Red Book). *ESA document reference ESA-SCI-DIR-RP-003*. Retrieved from https://www.cosmos.esa.int/documents/10892653/0/EnVision+Red+Book_ESA-SCI-DIR-RP-003+%281%29.pdf/

Fast, J. D., Gustafson, W. I., Easter, R. C., Zaveri, R. A., Barnard, J. C., Chapman, E. G., et al. (2006). Evolution of ozone, particulates, and aerosol direct radiative forcing in the vicinity of Houston using a fully coupled meteorology-chemistry-aerosol model. *Journal of Geophysical Research*, *111*(D21), 2005JD006721. https://doi.org/10.1029/2005JD006721

Gao, P., Zhang, X., Crisp, D., Bardeen, C. G., & Yung, Y. L. (2014). Bimodal distribution of sulfuric acid aerosols in the upper haze of Venus. *Icarus*, *231*, 83–98. https://doi.org/10.1016/j.icarus.2013.10.013

Gelbard, F. (1990). Modeling multicomponent aerosol particle growth by vapor condensation. *Aerosol Science and Technology*, *12*(2), 399–412. https://doi.org/10.1080/02786829008959355

Gillmann, C., Way, M. J., Avice, G., Breuer, D., Golabek, G. J., Höning, D., et al. (2022). The long-term evolution of the atmosphere of Venus: Processes and feedback mechanisms: Interior-exterior exchanges. *Space Science Reviews*, *218*(7), 56. https://doi.org/10.1007/s11214-022-00924-0

Imamura, T., & Hashimoto, G. L. (2001). Microphysics of Venusian clouds in rising tropical air. *Journal of the Atmospheric Sciences*, *58*(23), 3597–3612. https://doi.org/10.1175/1520-0469(2001)058<3597:MOVCIR>2.0.CO;2

Jacobson (2005). *Fundamentals of atmospheric modeling*. Cambridge University Press.

Jacobson, M. Z., Kaufman, Y. J., & Rudich, Y. (2007). Examining feedbacks of aerosols to urban climate with a model that treats 3-D clouds with aerosol inclusions. *Journal of Geophysical Research*, *112*(D24), 2007JD008922. https://doi.org/10.1029/2007JD008922

Jacobson, M. Z. (1997a). Development and application of a new air pollution modeling system—II. Aerosol module structure and design. *Atmospheric Environment*, *31*(2), 131–144. https://doi.org/10.1016/1352-2310(96)00202-6

Jacobson, M. Z. (1997b). Numerical techniques to solve condensational and dissolutional growth equations when growth is coupled to reversible reactions. *Aerosol Science and Technology*, *27*(4), 491–498. https://doi.org/10.1080/02786829708965489

Jacobson, M. Z. (2002). Analysis of aerosol interactions with numerical techniques for solving coagulation, nucleation, condensation, dissolution, and reversible chemistry among multiple size distributions. *Journal of Geophysical Research*, *107*(D19). https://doi.org/10.1029/2001JD002044

Jacobson, M. Z., Turco, R. P., Jensen, E. J., & Toon, O. B. (1994). Modeling coagulation among particles of different composition and size. *Atmospheric Environment*, *28*(7), 1327–1338. https://doi.org/10.1016/1352-2310(94)90280-1

James, E. P., Toon, O. B., & Schubert, G. (1997). A numerical microphysical model of the condensational Venus cloud. *Icarus*, *129*(1), 147–171. https://doi.org/10.1006/icar.1997.5763

Karyu, H. (2025). Dataset of "A Microphysics Model of Multicomponent Venus' Clouds with a High-Accuracy Condensation Scheme" Karyu et al. (2025) [Dataset]. *Zenodo*. https://doi.org/10.5281/zenodo.14600375

Karyu, H., Kuroda, T., Imamura, T., Terada, N., Vandaele, A. C., Mahieux, A., & Viscardy, S. (2024). One-dimensional microphysics model of Venusian clouds from 40 to 100 km: Impact of the middle-atmosphere eddy transport and SOIR temperature profile on the cloud structure. *The Planetary Science Journal*, *5*(3), 57. https://doi.org/10.3847/PSJ/ad25f3

Karyu, H., Kuroda, T., Itoh, K., Nitta, A., Ikeda, K., Yamamoto, M., et al. (2023). Vertical-wind-induced cloud opacity variation in low latitudes simulated by a Venus GCM. *Journal of Geophysical Research: Planets*, *128*(2), e2022JE007595. https://doi.org/10.1029/2022JE007595

Kasten, F. (1968). Falling speed of aerosol particles. *Journal of Applied Meteorology*, *7*(5), 944–947. https://doi.org/10.1175/1520-0450(1968)007<0944:fsoap>2.0.co;2

Knollenberg, R. G., & Hunten, D. M. (1980). The microphysics of the clouds of Venus: Results of the Pioneer Venus particle size spectrometer experiment. *Journal of Geophysical Research*, *85*(A13), 8039–8058. https://doi.org/10.1029/JA085iA13p08039

Kulmala, M., & Laaksonen, A. (1990). Binary nucleation of water–sulfuric acid system: Comparison of classical theories with different H_2SO_4 saturation vapor pressures. *The Journal of Chemical Physics*, *93*(1), 696–701. https://doi.org/10.1063/1.459519

Limaye, S. S., Grassi, D., Mahieux, A., Migliorini, A., Tellmann, S., & Titov, D. (2018). Venus atmospheric thermal structure and radiative balance. *Space Science Reviews*, *214*(5), 1–71. https://doi.org/10.1007/s11214-018-0525-2

Mahieux, A., Viscardy, S., Yelle, R. V., Karyu, H., Chamberlain, S., Robert, S., et al. (2024). Unexpected increase of the deuterium to hydrogen ratio in the Venus mesosphere. *Proceedings of the National Academy of Sciences*, *121*(34), e2401638121. https://doi.org/10.1073/pnas.2401638121

Mann, G. W., Carslaw, K. S., Ridley, D. A., Spracklen, D. V., Pringle, K. J., Merikanto, J., et al. (2012). Intercomparison of modal and sectional aerosol microphysics representations within the same 3-D global chemical transport model. *Atmospheric Chemistry and Physics*, *12*(10), 4449–4476. https://doi.org/10.5194/acp-12-4449-2012

Matsui, H. (2017). Development of a global aerosol model using a two-dimensional sectional method: 1. Model design. *Journal of Advances in Modeling Earth Systems*, *9*(4), 1921–1947. https://doi.org/10.1002/2017MS000936

McGouldrick, K. (2017). Effects of variation in coagulation and photochemistry parameters on the particle size distributions in the Venus clouds. *Earth Planets and Space*, *69*(1), 161. https://doi.org/10.1186/s40623-017-0744-x

McGouldrick, K., & Barth, E. L. (2023). The influence of cloud condensation nucleus coagulation on the Venus cloud structure. *The Planetary Science Journal*, *4*(3), 50. https://doi.org/10.3847/PSJ/acbdf8

McGouldrick, K., & Toon, O. (2007). An investigation of possible causes of the holes in the condensational Venus cloud using a microphysical cloud model with a radiative-dynamical feedback. *Icarus*, *191*(1), 1–24. https://doi.org/10.1016/j.icarus.2007.04.007

Mohs, A. J., & Bowman, F. M. (2011). Eliminating numerical artifacts when presenting moving center sectional aerosol size distributions. *Aerosol and Air Quality Research*, *11*(1), 21–30. https://doi.org/10.4209/aaqr.2010.06.0046

Petters, M. D., & Kreidenweis, S. M. (2007). A single parameter representation of hygroscopic growth and cloud condensation nucleus activity. *Atmospheric Chemistry and Physics*, *7*(8), 1961–1971. https://doi.org/10.5194/acp-7-1961-2007

Pruppacher, H. R., & Klett, J. D. (1997). *Microphysics of clouds and precipitation*. Springer.

Riemer, N., Ault, A. P., West, M., Craig, R. L., & Curtis, J. H. (2019). Aerosol mixing state: Measurements, modeling, and impacts. *Reviews of Geophysics*, *57*(2), 187–249. https://doi.org/10.1029/2018RG000615

Seiff, A., Schofield, J. T., Kliore, A. J., Taylor, F. W., Limaye, S. S., Revercomb, H. E., et al. (1985). Models of the structure of the atmosphere of Venus from the surface to 100 kilometers altitude. *Advances in Space Research*, *5*(11), 3–58. https://doi.org/10.1016/0273-1177(85)90197-8

Seinfeld, J. H., & Pandis, S. N. (2016). *Atmospheric chemistry and physics: From air pollution to climate change*. John Wiley & Sons.

Stolzenbach, A., Lefèvre, F., Lebonnois, S., & Määttänen, A. (2023). Three-dimensional modeling of Venus photochemistry and clouds. *Icarus*, *395*, 115447. https://doi.org/10.1016/j.icarus.2023.115447

Takagi, S., Mahieux, A., Wilquet, V., Robert, S., Vandaele, A. C., & Iwagami, N. (2019). An uppermost haze layer above 100 km found over Venus by the SOIR instrument onboard Venus Express. *Earth Planets and Space*, *71*, 1–12. https://doi.org/10.1186/s40623-019-1103-x

Titov, D. V., Ignatiev, N. I., McGouldrick, K., Wilquet, V., & Wilson, C. F. (2018). Clouds and Hazes of Venus. *Space Science Reviews*, *214*(8), 126. https://doi.org/10.1007/s11214-018-0552-z

Toon, O. B., Turco, R. P., Westphal, D., Malone, R., & Liu, M. (1988). A multidimensional model for aerosols: Description of computational analogs. *Journal of the Atmospheric Sciences*, *45*(15), 2123–2144. https://doi.org/10.1175/1520-0469(1988)045<2123:AMMFAD>2.0.CO;2

Turco, R. P., Hamill, P., Toon, O. B., Whitten, R. C., & Kiang, C. S. (1979). A one-dimensional model describing aerosol formation and evolution in the stratosphere: I. Physical processes and mathematical analogs. *Journal of the Atmospheric Sciences*, *36*(4), 699–717. https://doi.org/10.1175/1520-0469(1979)036<0699:AODMDA>2.0.CO;2

Vehkamäki, H., Kulmala, M., Napari, I., Lehtinen, K. E. J., Timmreck, C., Noppel, M., & Laaksonen, A. (2002). An improved parameterization for sulfuric acid–water nucleation rates for tropospheric and stratospheric conditions. *Journal of Geophysical Research*, *107*(D22). https://doi.org/10.1029/2002JD002184

Wilquet, V., Drummond, R., Mahieux, A., Robert, S., Vandaele, A. C., & Bertaux, J. L. (2012). Optical extinction due to aerosols in the upper haze of Venus: Four years of SOIR/VEX observations from 2006 to 2010. *Icarus*, *217*(2), 875–881. https://doi.org/10.1016/j.icarus.2011.11.002

Wilquet, V., Fedorova, A., Montmessin, F., Drummond, R., Mahieux, A., Vandaele, A. C., et al. (2009). Preliminary characterization of the upper haze by SPICAV/SOIR solar occultation in UV to mid-IR onboard Venus Express. *Journal of Geophysical Research*, *114*(E9). https://doi.org/10.1029/2008JE003186

Young, A. T. (1973). Are the clouds of Venus sulfuric acid? *Icarus*, *18*(4), 564–582. https://doi.org/10.1016/0019-1035(73)90059-6

Zeleznik, F. J. (1991). Thermodynamic properties of the aqueous sulfuric acid system to 350 K. *Journal of Physical and Chemical Reference Data*, *20*(6), 1157–1200. https://doi.org/10.1063/1.555899

Zhang, Y., Seigneur, C., Seinfeld, J. H., Jacobson, M. Z., & Binkowski, F. S. (1999). Simulation of aerosol dynamics: A comparative review of algorithms used in air quality models. *Aerosol Science and Technology*, *31*(6), 487–514. https://doi.org/10.1080/027868299304039